Materials and Design 31 (2010) 1790–1798

Contents lists available at ScienceDirect

Materials and Design

journal homepage: www.elsevier.com/locate/matdes

Influence of notch radius and microstructure on the fracture behavior of Al–Zn–Mg–Cu alloys of different purity

M. Vratnica [a,*], G. Pluvinage [b], P. Jodin [b], Z. Cvijović [c], M. Rakin [c], Z. Burzić [d]

[a] Faculty of Metallurgy and Technology, University of Montenegro, Džordža Vašingtona BB, 20000 Podgorica, Montenegro
[b] LABPS/LFM ENIM, University of Metz, Ile du Saulcy, 57045 Metz, France
[c] Faculty of Technology and Metallurgy, University of Belgrade, Karnegijeva 4, 11120 Belgrade, Serbia
[d] Military Technical Institute, Ratka Rešanovića 1, 11000 Belgrade, Serbia

ARTICLE INFO

Article history:
Received 10 July 2009
Accepted 7 November 2009
Available online 12 November 2009

Keywords:
Notch radius
Fracture behavior
Microstructure Al–Zn–Mg–Cu alloys

ABSTRACT

The influence of notch radius on the fracture behavior of two high-strength Al–Zn–Mg–Cu alloys with different Fe content in the T73 condition was investigated. The fracture toughness tests were performed on non-fatigue-precracked notched bending specimens with different notch radii ranged from 0.15 mm to 1.0 mm. The obtained data were interpreted using the concept of *Notch Fracture Mechanics* combined with finite-element method (FEM) calculations. It was found that both alloys are very sensitive to the notch radius. The fracture toughness increases with increasing notch radius. For a given notch radii, the increase in fracture toughness is more significant for the more pure alloy. The fracture behavior of investigated alloys with respect to microstructural features and their relation with the fracture micromechanisms were analyzed.

1. Introduction

Fracture in all materials, brittle or ductile, homogeneous or composites, is governed more or less by microscopic discontinuities and imperfections, such as, cracks, inclusions or dispersed phases [1]. Fracture toughness is a crucial material design criterion for many high strength materials applications [2]. In order to predict fracture toughness properties, accurate knowledge of the various influential parameters is required. However, careful experimentation is necessary for obtaining valid fracture toughness data and for comparing model predictions to experimental data.

Namely, it is well known that the fracture toughness test properties are also dependent on the notch geometry, which can be described by three parameters: the notch radius, the notch angle and the notch length [3–5]. Although the notch effects on fracture behavior of many materials were investigated, there still remain problems including uncertainties in the selection criteria of the notch geometry. Thus, for more precise analysis of fracture properties of high-strength Al–Zn–Mg–Cu alloys of 7xxx series further studies are needed to better understand the role of notch radius in the fracture toughness evaluation. Particularly in these alloys, finding wide applications in aircraft and spacecraft structures, fracture toughness is critical. The fracture toughness properties of this series of aluminum alloys can be improved by overaging in the T73 temper. However, many factors have been shown to influence their fracture toughness [6,7]. Among them, the microstructural factors such as type, volume fraction and morphology of intermetallic (IM) particles, grain size and geometry of precipitate-free zones (PFZs) are known to exert significant effects [8,9]. The previous studies [7–9] evidenced that they are responsible for the coexistence of different fracture micromechanisms. Since the fracture toughness level is strongly dependent on the relative contributions of these micromechanisms to the overall fracture, it is of interest to understand how different microstructural factors affect fracture toughness properties of a high-strength Al–Zn–Mg–Cu alloys having, generally speaking, the cracks of various sharpness. In this context, the coarse IM particles (typically Fe- or Si-containing phases [10,11]) with sizes larger than 1 μm [12], are especially important because the crack initiation and propagation are fostered by these brittle particles. Since their quantity is directly proportional to the Fe and Si impurity content [13–15], the fracture toughness increases with the increase of alloy purity. To characterize this correlation, precise and reliable fracture toughness evaluation is needed.

In the present study, the influence of notch radius on fracture toughness of overaged Al–Zn–Mg–Cu alloys having different purity was considered. The fracture toughness analysis was conducted using a *Notch Fracture Mechanics* approach [16,17], in which attention is focussed to explore the fracture parameters at the notch tip. The purpose of used two-step artificial ageing treatment was to obtain fracture toughness similar to the T73 condition, which is preferred in number design applications [18]. The obtained results

* Corresponding author: Tel./fax: +382 20 245 406.
E-mail address: majav@ac.me (M. Vratnica).

0261-3069/$ - see front matter © 2009 Elsevier Ltd. All rights reserved.
doi:10.1016/j.matdes.2009.11.018

were then compared to an extensive experimental study, which details have been published elsewhere [19,20]. This study provides the measurement of plane-strain fracture toughness K_{Ic} in the same situations (alloys composition, microstructural conditions and test orientation), quantitative values for microstructural parameters, fracture modes and tensile properties, which allow a validation of proposed micromechanical model for prediction of K_{Ic}. The relationships between fracture toughness, microstructure and micromechanisms of fracture in overaged Al–Zn–Mg–Cu plates were also discussed here.

2. Material, testing procedures and computing

Two commercial alloys supplied as hot-forged pancake-type plates were used in the present experiment. Their chemical compositions are given in Table 1. The both alloys belong to the maximal alloying group of 7xxx series. Differences in the microstructural factors were attained by variations in the Zn/Mg ratio and Fe impurity content. The Fe contet in the first alloy is low and almost half that in the second alloy. The plates were subjected to the following solution and ageing heat treatment: 460 °C/1 h + water quench + 100 °C/5 h + 160 °C/5 h. Detailed information on the processing of investigated plates is given in Ref. [19].

All investigations were performed at room temperature in radial-longitudinal (R–L) orientation. The microstructure of each plate was characterized in our previous works [19,20]. Optical microscopy (OM) and transmission electron microscopy (TEM) were employed. The specimens for OM were polished and chemically etched in the Keller's reagent. Thin foils for TEM were prepared by twin-jet electropolishing, using the Kestel's electrolyte followed by ionic polishing. The TEM observations and energy-dispersive spectrometer (EDS) microanalysis were performed using a TECHNAI F20S-TWIN transmission electron microscope with a field emission gun (FEG). The microstructure of both alloys consists of differently sized IM particles inhomogeneously distributed within the matrix (Fig. 1). They are of the following types: (a) coarse η-Mg(Zn, Cu, Al)$_2$, S-CuMgAl$_2$, Mg$_2$Si, Al$_7$Cu$_2$Fe and (Cu, Fe, Mn)Al$_3$ particles which are aligned as stringers, (b) coarse intragranular η-Mg(Zn,Cu,Al)$_2$ precipitates, (c) Mn-, Cr- and Zr-rich dispersoids, (d) quench-induced intra- and intergranular η-MgZn$_2$ precipitates, and (e) fine strengthening η-MgZn$_2$ precipitates. Microstructural parameters, such as the volume fraction, size and spacing of coarse IM particles and resolved precipitates, as well as the PFZs width and number were quantified by means of an image analysis.

Plane-strain fracture toughness tests were accomplished according to ASTM standard E399 on the fatigue-precracked three-point bending (SENB) specimens with the V notch [19,20]. The K_{Ic} values were determined indirectly from the critical value of J-integral, J_{Ic}, data by the following relation:

$$K_{Ic} = \sqrt{\frac{J_{Ic} \cdot E}{1 - \nu^2}} \tag{1}$$

where E is the Young's modulus and ν the Poisson ratio. The value of J_{Ic} was evaluated using the single specimen, elastic compliance method, according to ASTM standard E813. Validity requirements of K_{Ic} were met in both alloys. The broken K_{Ic} specimens were previously examined in a PHILIPS XL30 scanning electron microscope (SEM) to evaluate the fracture micromechanisms and reported elsewhere [19,20]. The fracture site was analyzed using the EDS to identify their origins. The area fractions of main fracture modes, A_A, were quantitatively assessed in the central region of the plastic zone ahead of the fatigue precrack where the stress state can be approximated by the plane-strain condition. The precision of the measurement can be estimated to ±10%. In order to determine yield strength σ_y, tensile tests were performed on the specimens of corresponding orientation according to ASTM standard E8.

To investigate the effects of notch radius on the toughness, SENB specimens with U notch, but no prior fatigue crack initiation, were employed. Five notch radii (ρ = 0.15, 0.30, 0.50, 0.80 and 1.0 mm) were used for the specimens with a length (L) of 120 mm, a thickness (B) of 10 mm, a width (W) of 20 mm and a notch length (a) of 10 mm. The fracture toughness was determined using the Volumetric method, where the stress distribution is computed to obtain an effective stress and an effective distance, and leads to the critical notch stress-intensity factor as a fracture toughness. *Notch Fracture Mechanics* extend the principles of (crack) fracture mechanics to notch, crack is then considered as a special case of notch. Volumetric method [17] is a meso fracture criterion method derived from *Notch Fracture Mechanics*. It is a two parameters fracture criterion taking into account the average stress value into the fracture process volume. The Volumetric method offers a specific method to determine the fracture process volume which is physically, the high stressed region. The limit of this region is an inflexion point on the opening stress distribution which corresponds to the zone where this distribution is governed by the notch stress intensity factor. Experimental proofs of the validity of this method are given in literature [17]. The averaging of the stress distribution into this volume can be simplified if we assumed that it is quasi-cylindrical by analogy with the notch plastic zone, which has a similar shape. The diameter of this cylinder is called the "effective distance" X_{ef}. The average stress value within the fracture process zone is then obtained by a line method which consists to average the opening stress distribution over the effective distance. One obtains the second fracture criterion parameter called the effective stress σ_{ef}. However, it is necessary to take into account the stress gradient due to loading mode and specimen geometry. This is done by multiply the stress distribution by a weight function $\Phi(r,\chi)$ where r is the distance from notch tip and χ the relative stress gradient defined by:

$$\chi(r) = \frac{1}{\sigma_{yy}(r)} \cdot \frac{\partial \sigma_{yy}(r)}{\partial r} \tag{2}$$

Several weights functions can be used including the unit and Peterson's weight function and are described in [17]. The effective stress is finally defined as the average of the weighted stress inside the fracture process zone:

$$\sigma_{ef} = \frac{1}{X_{ef}} \int_0^{X_{ef}} \sigma_{yy}(r) \cdot \Phi(r,\chi) dr \tag{3}$$

where σ_{ef}, X_{ef} and $\sigma_{yy}(r)$ are effective stress, effective distance and opening stress, respectively. The graphical representation of this local fracture stress criterion is given in Fig. 2, where the stress normal to the notch plane is plotted against the distance ahead of notch. In Fig. 2, the opening stress distribution versus distance is

Table 1
Chemical compositions of investigated alloys (mass%).

Alloy	Zn	Mg	Cu	Mn	Cr	Zr[a]	Ti[a]	Fe	Si	Al
1	7.45	2.47	1.53	0.25	0.17	0.15	0.015	0.12	0.11	Rest
2	7.65	2.26	1.55	0.25	0.18	0.11	0.017	0.26	0.11	

[a] Grain refining elements.

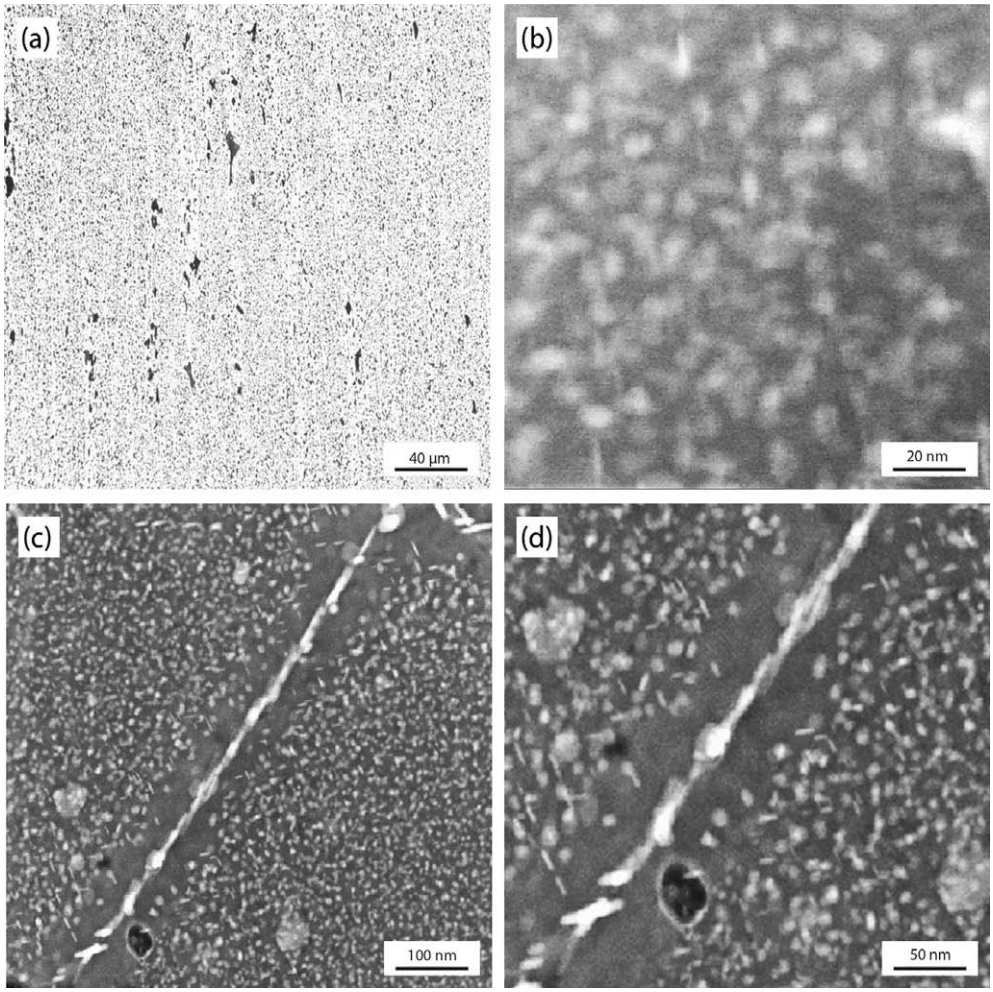

Fig. 1. Typical microstructure of overaged forgings: (a) OM micrograph of alloy 2 showing elongated dendrite arm boundaries with a significant number of coarse IM particles; (b), (c), (d) TEM micrographs of alloy 1 showing distribution of (b) intra precipitates, (c), (d) dispersoids, intra- and intergranular η precipitates.

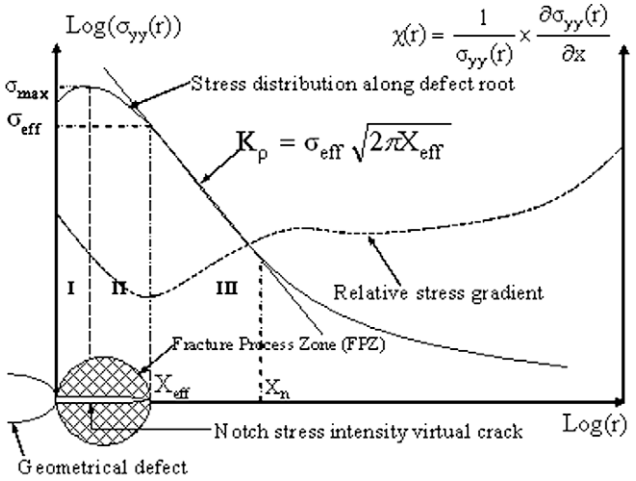

Fig. 2. Schematic presentation of a local stress criterion for fracture emanating from notches; determination of effective distance and the effective stress at notch tip together with the relative stress gradient vs. distance from the notch tip.

plotted in bi-logarithmic axes; the relative stress gradient is also plotted on the same graph. As it may be seen, the stress distribution at the notch tip decreases with the distance from the notch tip, and is characterised by three zones: the first one very near the notch tip, where the stress is constant and/or increasing to its maximum value; the second zone between the first and third zones; and the third, which can be simulated as a pseudo-stress singularity. For determination of X_{ef}, a graphical procedure is used; it has been observed that the effective distance is related to the minimum value of the relative stress gradient χ. Hence, the position of the minimum relative stress gradient allows obtaining an effective distance precise value. One notes on the same picture that the effective distance corresponds to stress distribution governs by a power law and fixed by a constant which is precisely the notch stress intensity factor defined from effective distance and stress by the following relationship:

$$K_\rho = \sigma_{ef}\sqrt{2\pi X_{ef}} \tag{4}$$

A simple fracture criterion is obtained by using the critical notch stress intensity factor $K_{\rho,c}$ and write:

$$K_\rho = K_{\rho,c} \tag{5}$$

The critical notch stress intensity factor is a fracture toughness with values in MPa $\sqrt{}$m units, if the notch has parallel side (notch angle equal to zero) and for elastic behavior.

The opening stress distribution at notch tip was computed using FEM with elasto-plastic material behavior by CASTEM® program for each test. A 3-dimensional FEM model mesh of one-half of the SENB specimen was constructed (see Appendix A). In the FEM

model, *x*-axis is parallel to the length of the specimen and perpendicular to the notch plane; *y*-axis is parallel to the height of the specimen and parallel to the notch plane; and *z*-axis is parallel to the thickness of the specimen and parallel to the notch plane. Triangular quadratic elements with six nodes were used. Elasto plastic computation has been achieved with the behavior law obtained from tensile experiments by ASTM E8-95 and introduced as data sets. Then a step-by-step procedure is applied which progressively converges to the solution. From this computation, the opening stress distribution along the ligament is extracted in view of the volumetric method application.

3. Results and discussion

The tensile and fracture toughness tests results are summarized in Table 2. The alloy 1 shows lower yield strength than the alloy 2, but higher toughness. Fig. 3 shows the critical notch stress intensity factor $K_{\rho,c}$ versus the square root of the notch radius curves for both alloys. It can be distinguished three zones: the first, where $K_{\rho,c}$ is approximately equal to K_{1c}, the second where $K_{\rho,c}$ varies linearly with the square root of ρ, and the third where $K_{\rho,c}$ is quasi independent on ρ. For both alloys, the fracture toughness of a notched specimen ($K_{\rho,c}$) is higher than the fracture toughness of a cracked specimen (K_{Ic}) because additional plastic work is dissipated in the notch plastic zone. This notch plastic zone increases with increasing notch radius, ρ, as a power function. However, for notch radius less than a critical value, ρ_c, the notch plastic zone is less than the fracture process zone and no extra plastic work is dissipated. Therefore, the fracture toughness is constant. On the other hand, if the notch radius increases enough, the ligament under notch is fully plastic and the work done for fracture does not increase. This appears for $\rho = \rho_p$ (ρ_p is the notch radius at the onset of ductile plateau). It has been noted by Morozov and Pluvinage [21] that the strain energy release rate described as a path integral called *M* is proportional to notch radius:

$$M = \frac{1}{4E} \cdot \pi \cdot \rho \cdot \sigma_{\max}^2 \tag{6}$$

where *E* is the Young's modulus and $\sigma_{\max}$ is the maximum stress at notch tip. Therefore, the critical notch stress intensity factor is proportional to the square root of the notch radius. Between these two situations, $K_{\rho,c}$ varies linearly with the square root of ρ. Those three parts are summarized by the following equations (7) to (9):

$$K_{\rho,c} \sim K_{Ic} \quad \text{for } \rho < \rho_c \tag{7}$$

$$K_{\rho,c} = m\sqrt{\rho} \quad \text{for } \rho_c < \rho < \rho_p \tag{8}$$

$$K_{\rho,c} = K_p \quad \text{for } \rho > \rho_p \tag{9}$$

where *m* is the notch sensitivity and K_p is the fracture toughness at ductile plateau. As shown in Fig. 3, fracture toughness increases linearly with the square root of the notch radius and reaches a constant value which is higher for alloy 1. The notch sensitivity *m* is higher for alloy 1 ($m = 93000\ \text{MPa}/\sqrt{\text{m}}$) than for alloy 2 ($m = 67800\ \text{MPa}/\sqrt{\text{m}}$). The purer alloy 1 has also the higher K_{Ic} fracture toughness. For both alloys, the ductile plateau is reached for $\rho = 0.8$ mm. Similar evolution was observed in steel [16] and in very brittle materials like glass [5]. The lower plateau cannot be clearly identified due to the fact that K_{Ic} fracture toughness tests are not performed in similar stress state conditions. In fact, a critical value of notch radius below which fracture toughness is not dependent on the notch radius can be measured. Several authors showed this for cast steel and the alumina ceramic. Thus, Pluvinage and Dhiab [22] reported that for the same steel the critical notch radius is about 1 mm at 20°, while Nishida et al. [23] indicated that fracture toughness K_{Ic} of fine-grained polycrystalline alumine is independent on the notch sharpness for notch radii <10 μm.

Table 2
Measured values of tensile and fracture-mechanics characteristics as a function of the alloy purity.

Alloy	ρ (mm)					σ_y (MPa)	K_{Ic} (MPa $\sqrt{\text{m}}$)
	0.15	0.30	0.50	0.80	1.00		
$K_{\rho,c}$ (MPa $\sqrt{m}$)							
1	37.72	45.29	53.63	53.89	61.78	288	49.8
2	28.86	39.29	46.90	52.48	52.02	318	44.1

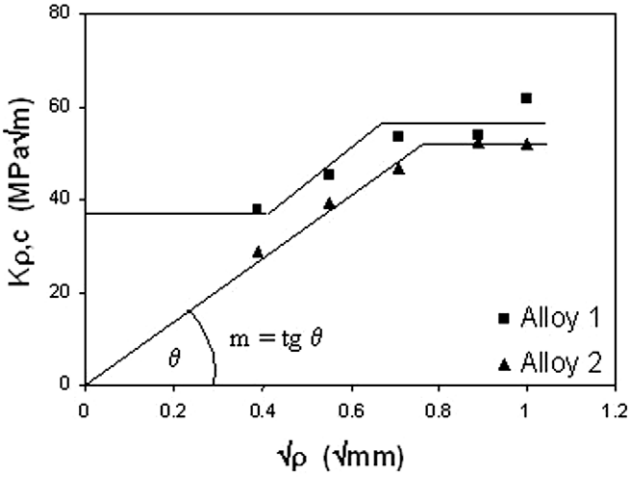

Fig. 3. Critical notch stress-intensity factor, $K_{c,}$ vs. the square root of the notch radius, ρ.

The critical notch radius depends on the yield strength of material. The decrease in the yield strength implies a decrease in the critical notch radius. In other words, the larger critical notch radii are detected for high-strength materials, *i.e.* materials with generally high notch sensitivity, rather than tough materials with lower yield strength [16]. Also, increasing the yield strength reduces the notch sensitivity. This is consistent with already observed difference in mechanical properties between the alloys 1 and 2 (see Table 2 and Fig. 3). Namely, the alloy 2 with higher Zn content shows higher yield strength and lower notch sensitivity as compared to the alloy 1. The better strength of alloy 2 indicates that Zn as main alloying element has a crucial role in determining the values of strength of the present alloys. As outlined in Ref. [24], the higher amount of Zn trapped in the matrix, the larger volume fraction of strengthening precipitates that can be obtained. This also illustrates that the strength properties are relatively unaffected by a change in microstructural parameters (Fig. 4a), resulting from different impurity level. Contrary to the strength situation, both fracture toughness, $K_{\rho,c}$ and K_{Ic}, are dependent on the alloy purity and its associated influences on the microstructural and fractographic characteristics (see Fig. 4). From Table 2 it is clear that toughness decreases in going from alloy 1 to alloy 2. Obtained data for K_{Ic} show that the presence of undesirable IM particles (coarse Fe-rich and Mg_2Si particles) in quantity for 0.298 vol.% greater in microstructure of alloy 2 compared to alloy 1, causes the drop in K_{Ic} value of ~12%. Since the Si content is constant, this implies that variations in the fracture toughness can occur with relatively small changes in the Fe content.

Namely, it is well known that the potential sites for fracture initiation are coarse IM particles, especially the Fe- and Si-rich phases having the lower fracture strength [25,26]. These brittle particles

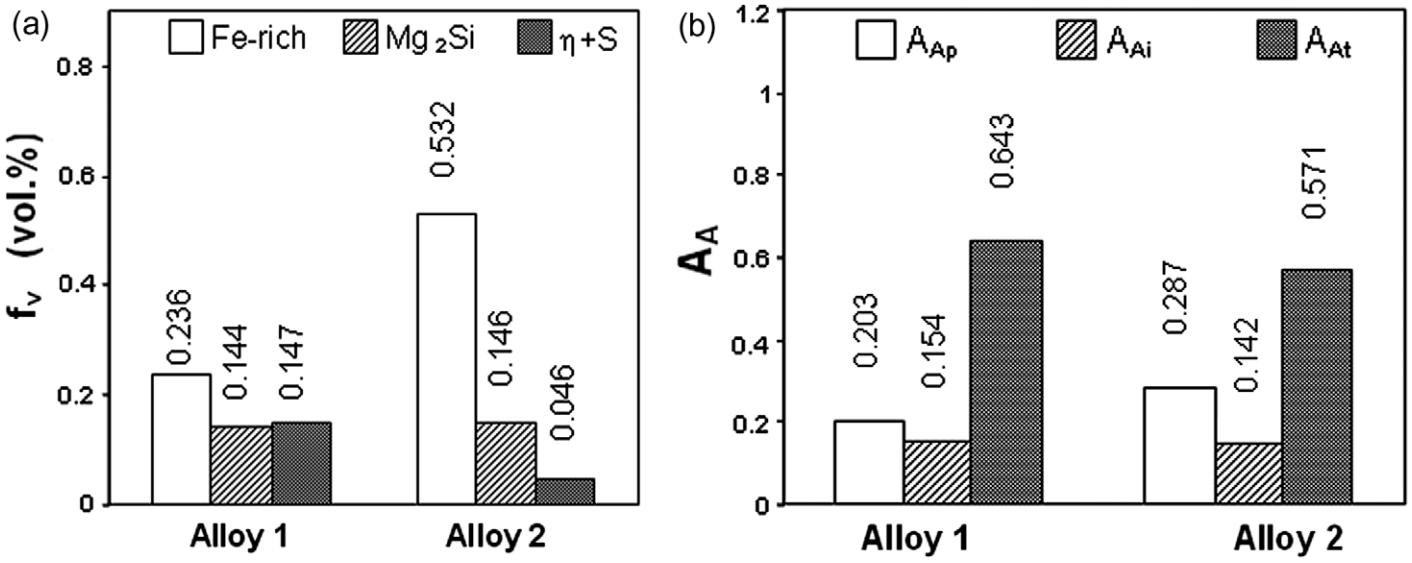

Fig. 4. (a) Volume fraction, f_v, of the coarse IM particles and (b) area fraction, A_A, of different fracture micromechanisms as a function of the alloy purity.

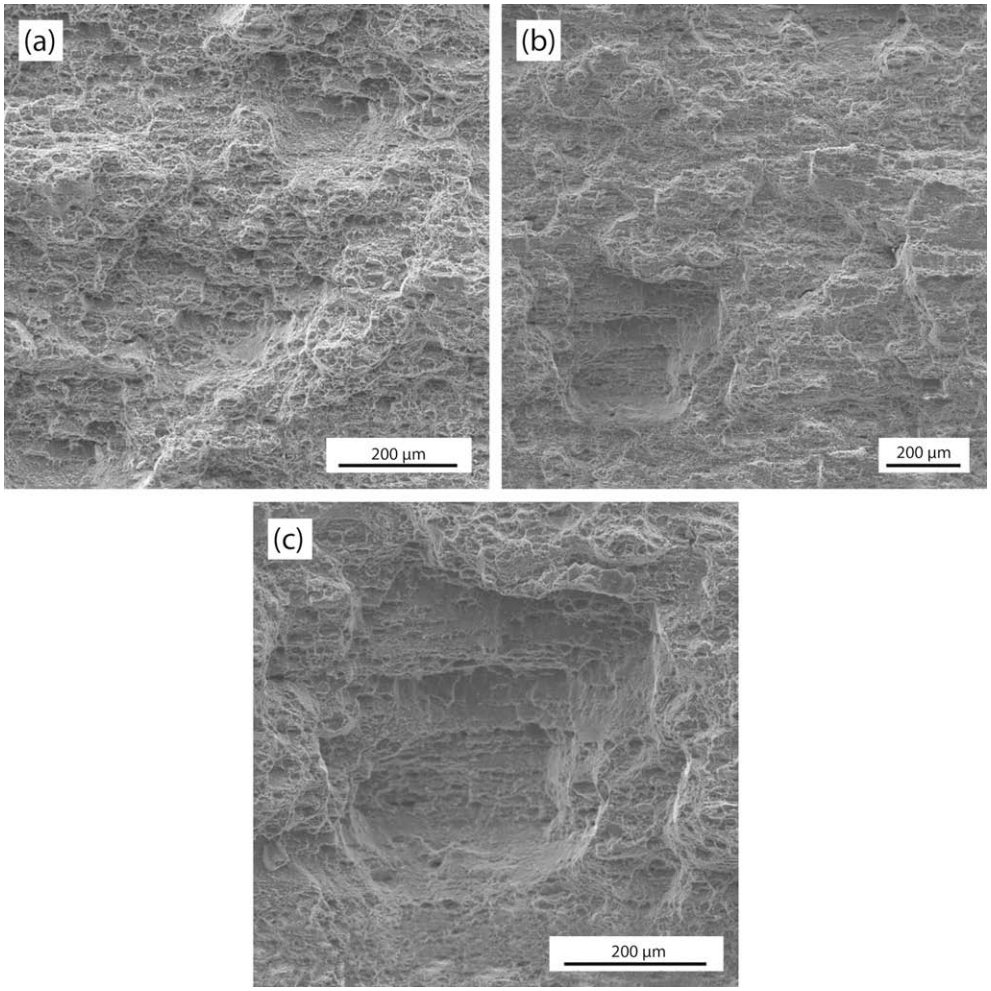

Fig. 5. SEM fractographs of broken K_{Ic} specimens showing overall morphology of fracture surfaces: (a) alloy 1; (b), (c) alloy 2.

fracture or separate from the matrix when the local normal stress exceeds a critical value [27–29], providing the preferential crack paths ahead of a crack. Their presence reduces the energy needed to propagate the advancing crack, causing a lower toughness. The differences in the fracture surface roughness of broken K_{Ic} specimens confirmed this hypothesis. As can be seen from Fig. 5, the

fracture of both alloys is ductile, but the macroscopic crack path or flatness of the fracture surfaces differs among the alloys. The fracture surface is more developed in the case of the alloy 1 (Figs. 5a and b). However, SEM observations at higher magnification revealed that all fracture surfaces are of ductile dimpled types, Fig. 6. Dimples are of different sizes. Large dimples, referred to as primary voids, always initiated at the coarse IM particles (Figs. 6a and c). Fine dimples, referred to secondary voids or microvoids, were found to initiate at medium-sized matrix precipitates (Fig. 6b). There are also very smooth zones, which are covered with smaller and shallow microvoids around precipitates assumed to be quench-induced intergranular precipitates. The flat regions with the higher number of coarse, primary voids were particularly noticed on the fracture surfaces of the alloy 2. Quantitative microstructural analysis data (Fig. 4a) showed that the higher percentage of coarse particles was estimated in the alloy 2, as a direct consequence of higher Fe content in this alloy. Thus, the f_v value of the Fe-rich phases increases proportionally from 0.236 to 0.532 vol.% with the increase in the Fe content from 0.12 mass% in alloy 1 to 0.26 mass% in alloy 2. As a result, the Fe-rich particles are coarser (2.37 μm compared to 2.08 μm for alloy 1) and distributed over distances that are about two times shorter than those in the more pure alloy 1, leading to reduction of the matrix capacity to deform. Although the particles of Mg_2Si phase are of average size from 1.92 μm in the alloy 1 to 2.09 μm in the alloy 2, they are present in much smaller and same amount (<0.15 vol.%) in the alloys, due to the smaller and equal Si content (0.11 mass%). In addition, coarse Mg_2Si particles exhibit a much smaller hardness than those of Fe-rich phases [26]. At the same time, increasing the Fe content decreased the volume fraction of soluble η and S phases, because some amounts of Cu combining with Fe are present in the form of various unsoluble Fe-rich phases. According to the image analysis, their volume fraction is quite different in the two alloys (Fig. 4a). However, η and S particles are much smaller than those of the Fe-rich and Mg_2Si phases, so that could show lower influence on the fracture processes. Since the unsoluble Al_7Cu_2Fe and (Cu, Fe, Mn)Al_3 phases are mostly found in the microstructure of both alloys, they should be more detrimental for toughness. As reported previously [19,20], the EDS analysis of various IM particles present on the fracture surface revealed that most of the Fe-rich particles are fractured, Fig. 6a and c. It was also observed that the large particles of Al_7Cu_2Fe, (Cu, Fe, Mn)Al_3 and Mg_2Si phases crack more often, while their smaller particle survive. This observation confirmed that the proportion of primary voids on the fracture surfaces associated with coarse IM particles is also dependent on the coarse particles size.

On the other hand, the Fe content does not affect the width of PFZs. These solute-depleted regions with average width of 1.87 to 1.90 μm, associated with the segregation of alloying elements during solidification and precipitation during applied heat treatment, lead to low plastic energy dissipation for intergranular fracture. The intergranular fracture is characterised by crack initiation and propagation along the grain boundaries covered with η-$MgZn_2$ precipitates accompanied by the PFZs (Figs. 1c and d) much softer

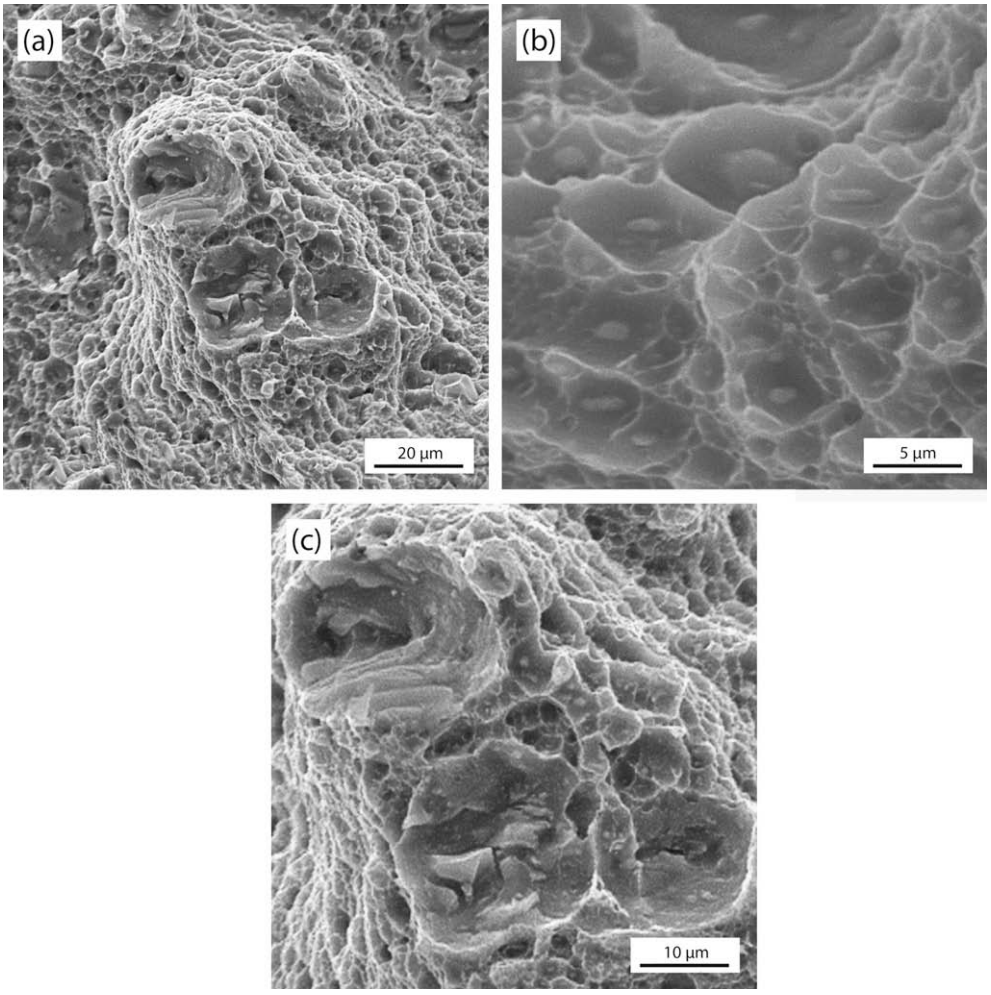

Fig. 6. SEM fractographs of broken K_{Ic} specimens of alloy 1 at a higher magnifications showing (a) typical overall morphology of fracture surfaces; (b) transgranular fracture area: fine population of small dimples around intragranular precipitates; (c) area of coarse primary voiding: large dimples around coarse IM particles.

than grain interior, promoting easier crack propagation within the PFZs. These intergranular precipitates confirmed by several studies [6,7,10,30] are coarser than the fine η-$MgZn_2$ precipitates a near-uniformly distributed within matrix, Fig. 1b. However, our studies [19,20] showed that the equilibrium η precipitates are also present within the grains. As mentioned above, it should be expected that the volume fraction of inter/intra precipitates is greater in alloy 2 than in alloy 1 [8,31]. This may have an influence on the proportion of microvoids initiation within the matrix and a competition process between transgranular fracture through the grain and intergranular fracture. Namely, transgranular fracture generated by decohesion of interface between the matrix and precipitates appeared to be dispersoids and other medium-sized phases within the grain (Fig. 6b) occurs in the ligaments that remain after the occurence of intergranular fracture. That the fracture path is influenced by the grain boundaries also indicates the presence of ridges (Fig. 5c). Instead, the matrix precipitation, which promotes transgranular fracture, is though to be dominant. A significant higher area fraction of transgranular fracture micromechanism, A_{At}, than those of intergranular fracture micromechanism, A_{Ai}, is estimated in both alloys, Fig 4b. On the other hand, the SEM fractographic analysis data shown in Fig. 4b also suggest that the failure occurs when the sum of the area fractions of the individual fracture modes (primary voiding at coarse IM particles, ductile intergranular and microvoid-induced transgranular fracture) is equal to 1 [11,32]:

$$(A_{Ap}) + (A_{Ai}) + (A_{At}) = 1 \tag{10}$$

where indexes *p*, *i* and *t* relate to fracture of coarse particles, intergranular and transgranular fracture, respectively. The relative contributions of these micromechanisms and, hence, toughness levels are dependent on the extent to which primary void growth continues prior to a secondary fracture mode (*i.e.* ductile intergranular or transgranular fracture), causing coalescence. Since an increase of the Fe content, which in turn increase the amount of coarse IM particles, leads to increased number of fractured particles, a competition between primary and secondary fracture is controlled mainly by the alloy purity. As shown in Fig. 4b, the relative contribution of primary voiding to the overall fracture process varies significantly with the Fe content. As the Fe content increases from alloy 1 to alloy 2 the area fraction of this fracture mode, A_{Ap}, increases from 0.203 to 0.287. The increase in the A_{Ap} causes a decrease in the A_{At} from 0.643 to 0.571. Since transgranular fracture involves significantly more plastic energy dissipation during fracture initiation in comparasion with fracture and decohesion of brittle IM particles or intergranular fracture, a decrease in the A_{At} decreases the total plastic energy dissipation. Consequently, the K_{Ic} decreases. Thus, the lower fracture toughness is achieved for the less pure alloy 2, which is characterised by the smaller proportion of transgranular fracture.

From the preceding analysis and results of present experiment, it is evident that the notch radius and alloy purity strongly affect the fracture behavior of high-strength 7xxx aluminum alloys. To obtain the suitable microstructure for the required fracture properties, it is necessary to introduce a comprehensive micromechanical model for fracture toughness prediction. Since the fracture process in high-strength 7xxx aluminum alloy products is very complex, most of existing models involve a variety of microstructural and micromechanical simplifications. More recently, we [19,20] proposed a multiple micromechanism-based model incorporating most important aspects of real fracture process in these alloys.

4. Fracture toughness prediction

Our model presented here is largely based on that derived by Hahn and Rosenfield [10], which has been extended to include the new microstructural and fractographic parameters controlling ductile intergranular and transgranular fracture. The attraction of this model is the fact that among proposed models only it describes fracture toughness in terms of the microstructural parameters associated with the coarse IM particles. This is of great importance, if it is known that the first step in the series of events leading to fracture is nucleation, growth and coalescence of voids at coarse particles. For a given yield strength σ_y, Hahn and Rosenfield model, which is expressed as:

$$K_{Ic} \approx \left[2\sigma_y E\left(\frac{\pi}{6}\right)^{1/3} D\right]^{1/2} f_v^{-1/6} \tag{11}$$

where D is the coarse particles diameter, f_v is their volume fraction and E is Young's modulus, predicts the experimental trend of a decrease in toughness with an increase in total volume fraction of coarse IM particles. It should be noted, however, that this model implies an increase in fracture toughness with increasing yield strength and particle size, which does not agree with the experimental results [33]. This is also contrary to our experiments. As can be seen from Table 3, the K_{Ic} values calculated using Eq. (11) significantly underestimated the measured K_{Ic} values reported in Table 2.

Therefore, Eq. (11) is modified, including A_{Ap} as a variable parameter. This extended model takes into account the decrease of total K_{Ic} with the increase of A_{Ap} and shows the correct inverse relationship of toughness-coarse particle size (as A_{Ap} generally decreases sharply with decreasing particle size). Further, the enhanced model is included in a complete model, considering all fracture modes. Following the approach of Gokhale et al. [32], an exponential dependence of K_{Ic} on the microstructural parameters affecting intergranular and transgranular fracture is used. Since the A_{Ai} is difficult to determine, the relative proportion of the intergranular fracture is given in term of the attributes associated with the PFZs. The proposed model predicts that fracture toughness depends on PFZs width (ω_{PFZs}). As the low yield stress in the PFZs leads to low plastic energy dissipation for intergranular initiation and propagation, the increase in the PFZs width decreases the fracture toughness. Also, the model predict that K_{Ic} increases with the square root of interparticle spacing (λ), one of the most important ingredients of the constitutive model. To calculate the dissipated energy for the intergranular fracture mode, a necessary parameter is the number (n) of PFZs observed between coarse IM particles distributed over λ distances. It is very difficult to reliably estimate the n value. For simplicity, we have chosen to let $n = 3$. This assumption is resonable because this PFZs parameter has a very limited influence on K_{Ic}. Finally, transgranular fracture contributing considerably more to toughness than intergranular fracture is given in term equal to A_{At}. Hence, the final model is a truly comprehensive model of fracture toughness, which is expressed as [19,20,34,35]:

$$K_{Ic} = \frac{K_{Icp}}{(A_{Ap})^m} \cdot \exp\left[(A_{At})^{1/2} \cdot \exp\left(-\left(\frac{n \cdot \omega_{PFZs}}{\lambda}\right)^{1/2}\right)\right] \tag{12}$$

where K_{Icp} denotes fracture toughness calculated using Eq. (11) and m is exponent depending on volume fraction of coarse IM particles.

Table 3
Calculated values of plane-strain fracture toughness as a function of the alloy purity.

Alloy	K_{Ic} (MPa $\sqrt{m}$)	
	Eq. (11)	Eq. (12)
1	21.4	48.2
2	21.5	40.4

The values of weight functions are based on the area fraction of the respective micromechanisms. Through establishment of corresponding dependences of K_{Ic} on the area fractions in logarithmic diagrams, the values of the exponents can be determined as the slopes of the straight lines used for linear regression for experimental points, if it is possible to represent these dependences by linear regression. This makes determination of the values of certain exponents impossible (see [32]). We have adopted constant values for the exponents of the microstructural parameters for intergranular and transgranular micromechanisms, considering small effect of these exponents on the K_{Ic}. Significant effect on K_{Ic} values has the exponent m. We have recommended two approximate values for m, following the increase of the value for m with the increase of A_{Ap} in the sum of the A_A of all three micromechanisms. In the case of alloy 1, m is anticipated to be 0.3. But, in the case of alloy 2 showing a large fraction of fractured particles, the value of m equals 0.5. Such an approach simplifies the application of proposed model. However, more accurate prediction of K_{Ic} requires that exponent m should be determined in the above mentioned way.

Validity of the Eq. (12) is verified using the measured values of basic tensile properties, microstructural and fractographic data presented in this article. The K_{Ic} values calculated by Eq. (12) are given in Table 3. The correlation between the predicted and measured toughness was good. Although the predicted values are lower than experimental ones, the deviation is relatively small and ranges from 1.6 MPa $\sqrt{}$m (alloy 1) to 3.7 MPa $\sqrt{}$m (alloy 2), representing only 3.2% or 8.4% of given K_{Ic} values.

The proposed model clearly shows the dominant influence of amount, size and density of coarse IM particles on fracture toughness of overaged forgings. These parameters are essentially controlled by the Fe content. Thus, the calculations show that some improvement in the fracture toughness is possible by decreasing the average size of Fe-rich particles. On the other hand, the experimental values of A_{Ap} and A_{At}, test the model prediction. However, since no model exists that can predict these fractions as a function of material properties, a necessary step is to model, in a predictive way, fracture mode occurrence as a function of the relevant microstructural parameters, which is difficult task.

5. Conclusions

Based on a study of the influence of notch radius and microstructural factors changed by the compositional variations on the fracture behavior of commercial Al–Zn–Mg–Cu alloys in the form of overaged forgings the following conclusions are provided:

1. Fracture behavior is very susceptible to the notch radius and the alloy purity.
2. The fracture toughness varies linearly with the square root of the notch radius. With increasing notch radius, fracture toughness increases. The increase in the fracture toughness is more significant for the more pure alloy. Increasing the yield strength reduces the notch sensitivity.
3. Fracture toughness is essentially controlled by the alloy purity, which in turn determines a volume fraction, size and spatial distribution of detrimental coarse IM particles, primarily Fe-rich phases. As the Fe content increases from 0.12 to 0.26 mass%, the amount of coarse particles that serve as the crack initiation sites increases from 0.236 to 0.532 vol.%. The area fraction of ductile transgranular fracture decreases with the increase in the volume fraction of coarse IM particles, while the area fraction of coarse voiding increases leading to a decrease in the toughness level. The K_{Ic} degradation is consistent with a change in the dominant fracture mode from secondary – transgranular to primary-coarse voiding at IM particles.
4. Using the proposed model it is possible to predict the fracture behavior when changes in relevant microstructural parameters and occurrence of fracture modes are observed. In practice, the

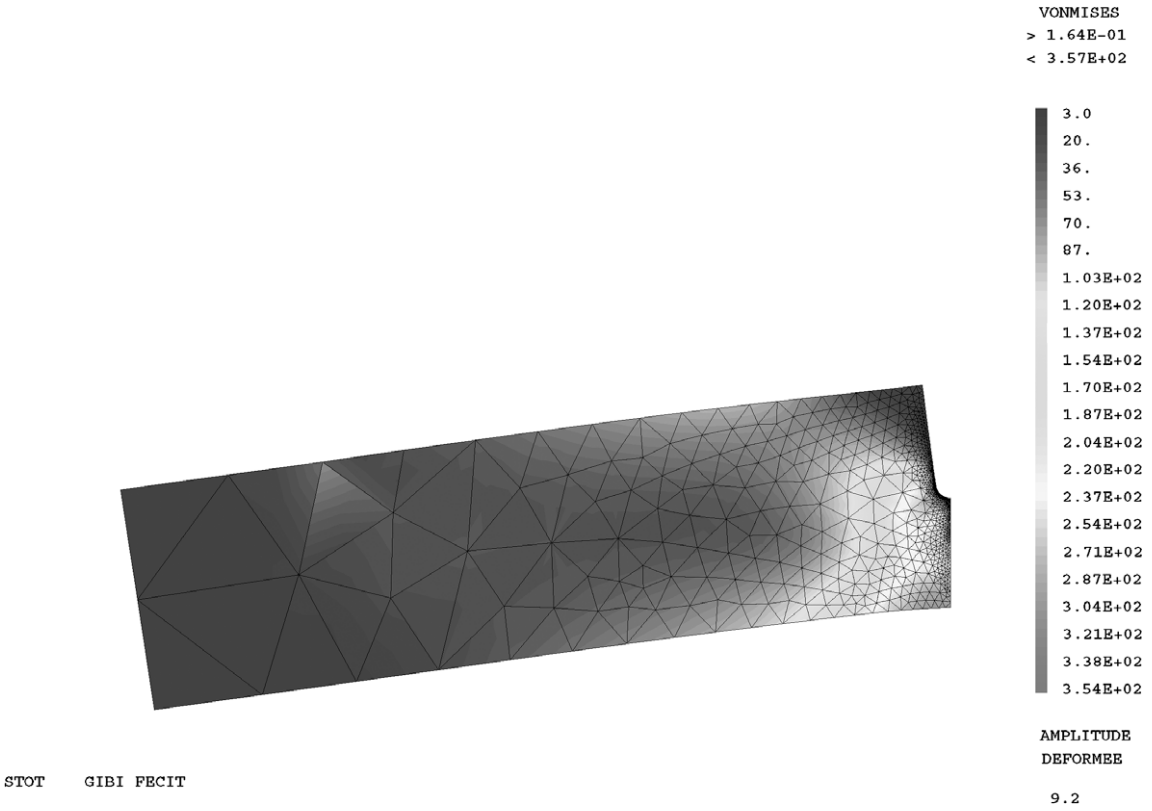

Fig. 7. Finite element mesh of full (one-half) SENB specimen.

model is applicable to industrial alloys in situations where a reduction in the amount of coarse IM particles, exerting an adverse effect on fracture toughness, and their size can be obtained by increasing the alloy purity, but also by controlling the content of main alloying elements.

Acknowledgements

The authors would like to acknowledge Institute ENIM of University of Metz for mechanical testing and Institute of Materials Science and Technology and USTEM of Technical University of Vienna for SEM and TEM experiments. The image analysis was performed at Faculty of Technology and Metallurgy of University of Belgrade with financially support from the Ministry of Science and Technological Development of the Republic of Serbia through the Project No. 144027.

Appendix A

The mesh, deformation and stress distribution on the half-specimen with a notch are shown in Fig. 7.

References

[1] Dash PK, Chatterjee AK. Effects of environment on fracture toughness of woven carbon/epoxy composite. IE (I) J – AS 2004;85:1–9.
[2] Morgeneyer TF, Starink MJ, Sinclair I. Evolution of voids during ductile crack propagation in an Al alloy sheet toughness test studied by synchrotron radiation computed tomography. Acta Mater 2008;56:1671–9.
[3] Pluvinage G, Gjonaj M. Notch effects in fatigue and fracture. London: Springer; 2001.
[4] Gilbert Kaufman J. Fracture resistance of aluminum alloys. The Aluminum Association: ASM International; 2001.
[5] Pluvinage G, Gilgert J. Fracture emanating from stress concentrators in materials: links with classical fracture mechanics. Mater in Tehn 2003;37:117–21.
[6] Morere B, Ehrström JC, Gregson PJ, Sinclair I. Microstructural effects on fracture toughness in AA 7010 plate. Metall Mater Trans A 2000;31A:2503–15.
[7] Dumont D, Deschamps A, Brechet Y. On the relationship between microstructure, strength and toughness in AA7050 aluminum alloy. Mater Sci Eng A 2003;356:326–36.
[8] Kamp N, Sinclair I, Starink MJ. Toughness-strength relations in the overaged 7449 Al-based alloy. Metall Mater Trans A 2002;33A:1125–36.
[9] Dorward RC, Beerntsen DJ. Grain structure and quench-rate effects on strength and toughness of AA 7050 Al–Zn–Mg–Cu–Zr alloy plate. Metall Mater Trans A 1995;26A:2481–4.
[10] Hahn GT, Rosenfield AR. Metallurgical factors affecting fracture toughness of aluminium alloys. Metall Trans A 1975;6A:653–67.
[11] Deshpande NU, Gokhale AM, Denzer DK, Liu J. Relationship between fracture toughness, fracture path, and microstructure of 7050 aluminum alloy: part I. Quantitative characterization.. Metall Mater Trans A 1998;29A:1191–201.
[12] Li XM, Starink MJ. Effects of compositional variations on characteristics of coarse intermetallic particles in overaged 7000 aluminium alloys. Mater Sci Technol 2001;17:1324–8.
[13] Ratzi R, Jeglitsch F, Kutner F. Gefüge und zähigkeiten in höchstfesten AlZnMgCu legierungen. Aluminium 1981;57:637–43.
[14] Ayer R, Koo JY, Steeds JW, Park BK. Microanalytical study of the heterogeneous phases in commercial Al–Zn–Mg–Cu alloys. Metall Trans A 1985;16A: 1925–36.
[15] Kovács-Csetényi E, Banizs K, Turmezey T, Šperlink K. Structure and properties of DC cast and extruded AlZnMgCu alloys with various impurity contents. Aluminium 1992;68:415–20.
[16] Pluvinage G, Šuštaršič B, Montannari F, Gilgert J, Leskovšek V, Vojvodič Tuma J. Fracture-mechanics characteristics of M-2-type high-speed steel. Mater Tehnol 2004;38:137–42.
[17] Pluvinage G. Fracture and fatigue emanating from stress concentrators. Kluwer Academic Publishers; 2003.
[18] Ou B-L, Yang J-G, Wei M-Y. Effect of homogenization and aging treatment on mechanical properties and stress-corrosion cracking of 7050 alloys. Metall Mater Trans A 2007;38A:1760–73.
[19] Cvijović Z, Rakin M, Vratnica M, Cvijović I. Microstructural dependence of fracture toughness in high-strength 7000 forging alloys. Eng Fract Mech 2008;75:2115–29.
[20] Cvijović Z, Vratnica M, Rakin M, Cvijović-Alagić I. Micromechanical model for fracture toughness prediction in Al–Zn–Mg–Cu alloy forgings. Philos Mag 2008;88:3153–79.
[21] Morozov E, Pluvinage G. Study of stress and strain concentration coefficient by path-integral. Problems of Strength, Special Publication 1996:53–64.
[22] Pluvinage G, Dhiab A. Notch sensitivity analysis on fracture toughness, transferability of fracture mechanical characteristics. Kluwer, NATO Sci Ser 2002;78:303–20.
[23] Nishida T, Hanaki Y, Pezzotti G. Effect of notch-root radius on the fracture toughness of a fine-grained alumina. J Am Ceram Soc 1994;77:606–8.
[24] Ferragut R, Somoza A, Tolley A. Microstructural evolution of 7012 alloy during the early stages of artificial ageing. Acta Mater 1999;47:4355–64.
[25] Toda H, Takahashi A, Kobayashi T. Effects of damaged coarse inclusion particles on mechanical properties of wrought aluminum alloys. Mater Sci Forum 2000;331–337:1261–6.
[26] Patton G, Rinaldi C, Brechet Y, Lormand G, Fongeres R. Study of fatigue damage in 7010 aluminum alloy. Mater Sci Eng A 1998;254:207–18.
[27] Staley JT. Influence of microstructure on fatigue and fracture of aluminium alloys. Aluminium 1979;55:277–81.
[28] Vratnica M, Cvijović Z, Degischer HP, Requena GC, Rumplmair G, Rakin M. Crack growth resistance of overaged Al–Zn–Mg–Cu alloys. Mater Sci Forum 2005;494:217–22.
[29] Vratnica M, Cvijović Z, Degischer HP, Requena GC. The effect of coarse intermetalic particles on the fracture process in forged 7000 alloy. J Micros 2006;224:117–20.
[30] Champlin J, Zakrajsek J, Srivatsan TS, Lam PC, Manoharan M. Influence of notch severity on the impact fracture behavior of aluminum alloy 7055. Mater Des 1999;20:331–41.
[31] Femminella OP, Starink MJ, Gunn SR, Harris CJ, Reed PAS. Neurofuzzy and SUPANOVA modelling of structure-property relationships in Al–Zn–Mg–Cu alloys. Mater Sci Forum 2000;331–337:1255–60.
[32] Gokhale AM, Deshpande NU, Denzer DK, Liu J. Relationship between fracture toughness, fracture path, and microstructure of 7050 aluminum alloy: part II. Multiple micromechanisms-based fracture fracture toughness model. Metall Mater Trans A 1998;29A:1203–10.
[33] Dumont D, Deschamps A, Brechet Y. A model for predicting fracture mode and toughness in 7000 series aluminium alloys. Acta Mater 2004;52: 2529–40.
[34] Vratnica M, Cvijović Z, Rakin M. Fracture toughness modelling in high-strength Al-based alloys. Mater Sci Forum 2004;453–454:181–6.
[35] Cvijović Z, Vratnica M, Rakin M. Micromechanical modelling of fracture toughness in overaged 7000 alloy forgings. Mater Sci Eng A 2006;434: 339–46.